Permselective ion electrosorption of subnanometer pores at high molar strength enables capacitive deionization of saline water

Sheng Bi,[1,2,+] Yuan Zhang,[3,4,+] Tangming Mo,[1,2] Luca Cervini,[5]
John M. Griffin,[5,6] Volker Presser,[3,4,*] Guang Feng[1,2,*]

[1] State Key Laboratory of Coal Combustion, School of Energy and Power Engineering, Huazhong University of Science and Technology (HUST), Wuhan 430074, China.

[2] Nano Interface Centre for Energy, School of Energy and Power Engineering, HUST, 430074, China.

[3] INM - Leibniz Institute for New Materials, Campus D2 2, 66123 Saarbrücken, Germany.

[4] Department of Materials Science and Engineering, Saarland University, Campus D2 2, 66123 Saarbrücken, Germany.

[5] Department of Chemistry, Lancaster University, Lancaster, LA1 4YB, United Kingdom.

[6] Materials Science Institute, Lancaster University, Lancaster, LA1 4YB, United Kingdom.

[+] These authors contributed equally: Bi Sheng, Yuan Zhang.

[*] Corresponding authors. Email: volker.presser@leibniz-inm.de (VP); gfeng@hust.edu.cn (GF)

Abstract

Capacitive deionization with porous carbon electrodes is an energy-efficient water treatment technique limited to the remediation of only brackish water due to the severe efficiency drop at high molar strength. Combining experiment and simulation, our work demonstrates the ability of subnanometer pores for permselective ion electrosorption, which enables capacitive deionization for saline media with high concentrations. Molecular dynamics simulations reveal the origin of permselective ion electrosorption in subnanometer pores at high molar strength. Within the subnanometer range, carbon pores with smaller size become more ionophobic and then express a higher ability of permselective ion electrosorption. This can be understood by the effects of the pore size on the microstructure of in-pore water and ions and the nanoconfinement effects on the ion hydration. These findings provide a new avenue for capacitive deionization of saline water (seawater-like ionic strength) to enable the application of highly concentrated saline media by direct use of porous carbons.

Keywords

Electrochemistry; water treatment; capacitive deionization; molecular dynamics; supercapacitor

1. Introduction

Advancing towards a sustainable future requires not only to improve our current ability for water management but also to afford energy-efficient water desalination.[1] With the rising demand for potable water, increased pollution, and global climate change, scientists explore advanced techniques for desalination.[2] Along these lines, capacitive deionization (CDI) is a still emerging water purification technique that provides energy-efficient desalination of brackish water.[3-6] The CDI process for water desalination relies on the accumulation of ions in polarized electrodes. By applying an electrical potential between two electrodes, cations and anions are removed from a water stream passing the electrochemical cell and respectively electro-adsorbed at the negatively and positively charged electrodes.[6-8] The mechanism of ion electrosorption is well-known in the field of electrical energy storage, which could be exemplified by electrical-double layer capacitors (also called supercapacitors) in many present-day devices, ranging from mobile applications to stationary (grid-scale) systems.[9-11] With the ability to use charge accumulation to desalinate saline media during the electrode charging process and to recover the electrical energy during electrode regeneration (discharging), CDI units are also uniquely qualified to contribute towards large-scale energy storage and grid management.[12-14]

The process of ion electrosorption favors porous electrode materials with a high specific surface area. Accordingly, CDI devices commonly employ porous carbons,[15-17] such as activated carbons,[18, 19] graphene-based materials,[20-22] carbon nanotubes,[23, 24] or carbon aerogels[25]. Like for supercapacitors,[26] micropores benefit the performance of CDI electrodes, compared to meso- or macropores.[27] However, the detailed understanding of the influence of the pore size on the desalination performance has remained limited. In part, this is caused by the pore size dispersity of carbon electrode materials, which complicates to deconvolute the individual processes occurring in different pores. Modeling ion electrosorption in pores of different sizes is, therefore, an important approach to quantify the behavior and properties of ions in nanoconfinement.[10, 27-30] With the majority of works in the field of supercapacitors using organic electrolytes or ionic liquids,[10, 31-33] quantitative analysis of ion electrosorption in carbon nanopores using aqueous media is still poorly investigated.[34, 35] The specific challenge for CDI modeling is the dependency of the desalination performance on the actual mode of charge storage.[36] Specially, we must consider the number of co-ions and counter-ions (that is, ions with same or opposite charge compared to the electrode), and their relative changes as

a function of the state of charge.

Different from the charge storage mechanism of supercapacitors, the non-permselective exchange of one cation by one anion during the charging of the positively polarized electrode (and vice versa at the negatively polarized electrode) fails to change the concentration of the effluent water stream.[30] Instead, desalination is only possible when the change of electro-adsorbed counter-ions exceeds that of electro-desorbed co-ions.[37] This fundamental correlation makes the desalination performance of CDI highly dependent on the bulk ion concentration. Carbons may accomplish at low molar strength of about 5-20 mM a desalination capacity of 10-30 mg/g,[7, 38-41] while many studies have revealed that at high molar strength (>50-100 mM), the charge storage process is dominated by non-permselective ion swapping, and thus effective desalination by CDI becomes impossible.[30, 34, 42] Only at molar strength below 50 mM, CDI becomes a promising energy-efficient desalination technology, which limits the technology to remediation of only brackish water.[16, 37, 43] Accordingly, the field of electrochemical desalination has moved away from carbon to explore electrode materials capable of ion insertion or conversion reactions.[44, 45] Such Faradaic processes could overcome the limitation of electrosorption and allow permselective and energy-efficient ion removal even at high molar strength (e.g., as found for seawater: 600 mM).[45-47]

Our work was motivated by going in the opposite direction: to turn back to carbon. More precisely, our study shows that as subnanometer-sized pores become more ionophobic, they gain the ability of permselective ion electrosorption at high molar strength. However, such effects have not been found experimentally or correlated with a combined experiment and simulation approach. We demonstrate this unexpected feature by molecular dynamics (MD) simulations, with constant potential to mimic the applied voltages on the electrode,[48, 49] that allow us to investigate carbon pores individually with charging process and by CDI experiments with activated carbon cloth with equally small pores at high molar strength. The pore-size dependent CDI ability of subnanometer pores and their molecular insights, as well as the origin of the permselective electrode, are clarified and discussed. Thereby, the current paradigm of limiting CDI to just brackish water could be reconsidered as: if appropriate nanopores are being employed, CDI is also capable of desalination of highly saline aqueous media. In this work, we focus mostly on potassium chloride (KCl) solution, considering the smaller size of hydrated potassium ion compared to hydrated sodium ion.[50] Thereby, we establish the ability to enable permselectivity in sodium chloride (NaCl) and at molar concentrations exceeding that of

seawater.

2. Simulation and experimental section

Molecular dynamics simulations. The electrode pore walls are modeled by fixing three layers of graphene sheets. The pore size, defined as the access width,[51] ranges from 0.47 nm to 1.77 nm. The pore length is set as 5.85 nm, which is long enough to eliminate the entrance effects on the central part of the pore.[52] The initial configurations of the KCl and NaCl solutions are obtained by randomly distributing ions and water molecules in the accessible space using PACKMOL.[53] The detailed numbers of the components (ions and water) in each case are gathered in *Supporting Information*, **Table S1**. For electrodes and aqueous KCl and NaCl electrolytes, we adopted force fields from Cornell et al.[54] and Smith et al.[55], respectively, and the well-established SPC/E model[56] was chosen for the water molecules.

Constant potential implementation. For all simulations, the constant potential method (CPM) was implemented to capture the electrode polarization effects in the presence of an aqueous electrolyte.[57] This method allows the fluctuation of electrode charge during the simulation so that a constant electrical potential between two electrodes could be maintained.[58-61] All simulations were performed in the NVT ensemble, using a customized MD package GROMACS[62] with a time step of 2 fs. The temperature of the electrolyte is maintained at 298 K using the V-rescale thermostat. A fast Fourier transform (FFT) grid spacing of 0.1 nm and cubic interpolation for charge distribution were used to compute the electrostatic interactions in the reciprocal space. We used a cutoff length of 1.2 nm in the calculation of electrostatic and non-electrostatic interactions in the real space. Each simulation started with an annealing process from 350 K to 298 K over a period of 10 ns, followed by another 10 ns to reach equilibrium. After that, a 40 ns production run was performed for analysis. For the sake of the accuracy of modeling, 10 runs were carried out with different initial configurations (i.e., with different locations and velocities of ions and water molecules) to obtain reliable results of charging dynamics.

Carbon electrodes materials. Four kinds of commercial activated carbon cloth (Kynol ACC-5092-10, Kynol ACC 5092-15, Kynol ACC 507-20, Kynol 507-20+, and Kuraray YP-80F) were applied as electrode materials in this work.[63] Among them, Kynol ACC-5092-10, Kynol ACC 5092-15, and Kynol ACC 507-20 and Kynol 507-20+ (labeled as ACC-0.59, ACC-0.67, ACC-0.88, and ACC-1.26) are novolac-derived activated carbon cloth with different degree of the

activation process and thickness of 650 µm, 450 µm, and 250 µm, respectively. Thereby, all ACC electrodes were free-standing and binder-free. 95 mass% of YP-80F (labeled AC-1.34) activated carbon material was mixed with 5 mass% polytetrafluoroethylene (PTFE, Sigma-Aldrich) to form a 650 µm thick, free-standing electrode.

Material characterization. Scanning electron micrographs (*Supporting Information*, **Figure S1**) were recorded with a JEOL JSM-7500F system at an acceleration voltage of 3 kV. The samples were mounted on sticky tape and analyzed without the aid of an additional, conductive sputter coating.

Nitrogen sorption experiments were performed with an Autosorb iQ system (Quantachrome) at -196 °C. The samples were degassed at 10^2 Pa at a temperature of 200 °C for 10 h. The specific surface area (SSA) and pore size distribution (*Supporting Information*, **Table S2**, *Supporting Information*, **Figure S2**) were calculated by applying quenched-solid density functional theory (QSDFT) assuming a slit-shaped pore model.[64, 65]

The chemical composition was quantified with a CHNS analyzer Vario Micro Cube from Elementar. The temperature for the tube was 850 °C and for the combustion tube 1150 °C. The equipment was calibrated with sulfanilamide. The oxygen content was obtained with a rapid OXY cube from Elementar. The analysis temperature was 1450 °C, and it was calibrated with benzoic acid. See *Supporting Information*, **Table S3**.

Desalination performance measurements. We used a symmetric full-cell configuration to evaluate the desalination performance. As shown in *Supporting Information*, **Figure S1**, carbon materials were cut into 30 mm diameter disks. The feed water flows through the middle channel, which is sandwiched by glass fiber separators (Millipore, 4 pieces of 380 µm) and activated carbon electrodes. To ensure that the space of the water-flowed middle channel does not collapse during the measurement, 7 pieces of polyethylene terephthalate cloth meshes (28 mm-diameter round pieces) were filled inside of the middle channel. This translates to a spacing of 3 mm between the two electrodes. The flow rate of the feedwater stream was set 5 mL/min. At the outlet of the cell, pH and conductivity sensors were connected to monitor the pH and concentration fluctuations during the electrochemistry measurements.

We used a Biologic VSP300 system to determine the electrochemical performance, a Metrohm PT1000 conductometric cell to monitor the electrolyte concentration, and the pH values were recorded with a WTW SensoLyt 900P sensor probe. By this way, we determined values for the

charge efficiency and desalination capacity. Galvanostatic charge and discharge cycling was carried out at a specific current of 0.1 A/g using different potential ranges, namely, 0-0.2 V, 0-0.4 V, 0-0.6 V, 0-0.8 V, and 0-1.0 V with 20 cycles for each potential range. After charging and discharging, 2 min of the potential holding time was applied. The electrode mass was as follows: 145 mg for ACC-0.59, 120 mg for ACC-0.67, 116 mg for ACC-0.88, 64 mg for ACC-1.26, and 172 mg for AC-1.36. The specific current applied was calculated from the total mass of both sides of electrode.

The desalination capacity (DC) was determined by **Eq. (1)**:

$$\mathrm{DC} = \left(\nu \cdot \frac{\mathrm{M_{salt}}}{\mathrm{m_{tot}}}\right) \int \ (\mathrm{c_t} - \mathrm{c_0})\mathrm{dt} \qquad \textbf{(Eq. 1)}$$

where v is the flow rate of salt solution, M_{salt} is the molecular mass of the salt, m_{tot} is the total mass of both working and counter electrode, and c_0 and c_t are initial concentration and concentration value at time t.

The charge efficiency (CE) was calculated by **Eq. (2)**:

$$\mathrm{CE}\ (\%) = \frac{F \cdot DC_{mol}}{\mathrm{Q}} \cdot 100\% \qquad \textbf{(Eq. 2)}$$

where F is the Faraday constant (in units of Ah/mol), Q is the invested charge (in units of Ah) including the leakage current, and DC_{mol} is the desalination capacity (in unit of mol).

In our experiments, the error margin for CE and DC was about 5-8%.

Solid-state nuclear magnetic resonance spectroscopy. We used a 400 MHz Bruker Avance III HD WB spectrometer operating at a magnetic field strength of 9.4 T. Before soaking in 800 mM aqueous NaCl, the samples were dried in an [vacuum?] oven at 80 °C overnight, and introduced in 3.2 mm zirconia rotors. The magic angle spinning (MAS) rate was 5 kHz. ^{1}H NMR spectra were acquired using the DEPTH pulse sequence[reference] with 16 scans phase cycle, 5 s recycle delay, and 90° pulse lengths of 3-3.3 µs at a power of 200 W. ^{23}Na MAS NMR spectra were recorded with a single pulse and 1014-20420 scans depending on the sample, recycle delays of 0.2 s, and 90° pulse lengths of 3.75-4.2 µs at a power of 200 W.

3. Results and Discussion

3.1. Capacitive deionization ability of micropores

The key working principle of CDI is demonstrated in **Figure 1a**: when saline feed water passes electrically charged electrodes, ions will be electro-adsorbed at the fluid-solid interfaces between the aqueous electrolyte and carbon nanopore surfaces. We first examine the ability of carbon electrodes with different pore sizes to accomplish capacitive deionization at high

molar strength even above standard seawater by using 800 mM KCl solution, although nanoporous carbons had shown the inability of activated carbon with pores >1 nm to accomplish any desalination in 600 mM NaCl solution while it worked well for supercapacitor.[42] Employing activated carbon cloth (ACC) and activated carbon (AC) as electrodes (*Supporting Information,* **Figure S1**), we labeled the samples by their average pore size, namely ACC-0.59 (average pore size is 0.59 nm), ACC-0.67 (0.67 nm), ACC-0.88 (0.88 nm), ACC-1.26 (1.26 nm) and AC-1.34 (1.34 nm). From the pore size distribution of these carbon materials (**Figure 1b** and *Supporting Information*, **Figure S2**), we observe the pronouncedly microporous characteristics of all studied ACCs, while the widest pore size distribution is found for AC-1.34 which also contains 13.8% mesopores (diameters within 2-50 nm; *Supporting Information*, **Table S2** provides more data from pore structure analysis). We chose nanoporous carbons with narrow pore size distribution because these specific carbons have a small amount of non-carbon heteroatoms and surface groups (chemical data can be found in *Supporting Information*, **Table S3**). **Figure 1c** shows the desalination capacity for aqueous 800 mM KCl normalized to the specific surface area of the different carbon electrodes at cell voltages up to 1.0 V. Herein, the use of area-normalized desalination capacities is more reasonable for a direct comparison of carbons with different surface area compared to mass-normalized values. In alignment with the reported CDI techniques,[30, 34, 42] we see the inability of carbon nanopores exceeding 1 nm to desalination even at the highest applied cell voltage. As the average pore size is decreased, there is a significant increase in areal desalination capacity with the highest value found for ACC-0.59 (4.58 µg/m^2 = 4.73 mg/g at 1.0 V). To the best of our knowledge, these data are the first reports of nanoporous carbons accomplishing actual desalination at high molar strength via CDI in the absence of an ion-exchange membrane. The ability for ion removal is also maintained when using 800 mM NaCl solution (*Supporting Information*, **Figure S3-4**).

To scrutinize desalination capacities, the charge efficiency is analyzed in **Figure 1d**, correlating the charge corresponding with removed salt ions and the total amount of invested charge. It can be seen that the charge efficiency even at the highest applied cell voltage of 1.0 V remains close to zero for pores larger than 1.2 nm on average (either ACC-1.26 or AC-1.34), however, when approaching and falling below the 1-nm-range, there is a significant increase in charge efficiency that aligns with the manifestation of desalination. Subnanometer pores at 1.0 V show a charge efficiency of about 36 % and this value also contains resistive charge losses of

the cell and its graphitic carbon current collectors. This charge efficiency seems small compared to activated carbons commonly used for CDI that provide 60-80% charge efficiency[16] but is very large compared to the performance of micropores exceeding an average of 1.2 nm. Also, considering the pore size dispersity (**Figure 1b**), there is an influence of larger pores even for the sample with the smallest average pore size and this may further contribute to a reduced charge efficiency. Theoretically, if all charges would be stored by a one-to-one cation-anion swapping process, no desalination would be observed (like in case of large micropores).[42] Yet, the unexpected ability of subnanometer pores to accomplish the actual desalination at high molar strength indicates a significant amount of ion permselectivity, that is, subnanometer pores have a growing preference of counter-ion electro-adsorption instead of co-ion electro-desorption. Such behavior agrees with some previous theoretical work on graphene nanochannels which up-take ions only when electrically charged.[49] It aligns also with the hindrance of ions such as Na^+ and Cl^- for monolayer water transport across ultrathin graphene channels.[66]

To understand the permselective ion electrosorption of subnanometer pores, we used molecular dynamics (MD) simulations to study the electrochemical operation of aqueous electrolyte at high molar strength. As shown in **Figure 2a**, we construct a three-dimensional periodical system with two slit-shaped micropores of adjustable size (d_{slit}) connected by reservoirs of bulk aqueous electrolyte. The constant potential method is implemented to maintain the potential drop between the two electrodes during the simulations.[58, 59] This computational method allows us to explore the processes of charge storage and dynamically monitor ion electro-sorption/desorption in micropores at the atomic level.[60, 61] As exemplified for all carbon electrode materials in this study by conventional electrochemical operation in a two-electrode cell in 2 M KCl, there is a capacitive response with a rectangular-shape cyclic voltammogram provided by porous carbons (*Supporting Information*, **Figure S5**), indicating the absence of electrochemically triggered redox reactions. Therefore, MD simulations with aqueous solutions at two high molar strengths (500 mM and 2 M) could be performed to investigate the dynamic process of ion electro-sorption/desorption and its permselectivity by carbon nanopores. As exhibited for the temporal change of ions in the negatively charged electrode in **Figure 2b** (results for positive electrode in *Supporting Information*, **Figure S6**), pores of 0.57 nm and 0.77 nm show almost exclusive counter-ion electro-adsorption at 1.0 V and avoidance of co-ions, while pores in larger size (0.97 nm and 1.37 nm) contain a much

larger number of co-ions. This trend holds for both 500 mM and 2.0 M aqueous KCl solutions under 1.0 V; however, for 500 mM, we see a much lower number of co-ions populating the pores during the charging process including its initial state. The change of in-pore ion population and charge stored on the pore translates to theoretical charge efficiency, as shown in **Figure 2c**. It can be found that the charge efficiency is enhanced with the decrease of either pore size or ion concentration, except its unit value in very small pores (<0.6 nm) due to the absence of ions at the initial state of charging process; the modeling-obtained values of charge efficiency are larger than experiment-measured ones, which may be contributed to the absence of pore size distribution and the simplification of pore surface geometry and chemistry in MD modeling. These findings are validated for different working potential and saline water (e.g., KCl and NaCl solutions under 1.5 V in *Supporting Information*, **Figure S7**), which qualitatively match with our experimental data (**Figure 1b,c**), documenting the ability for subnanometer pores to enable capacitive deionization in saline media with high molar strength (exceeding the ion concentration level of seawater). Our findings are in stark contrast to the current state-of-the-art assessment that membrane-free capacitive carbon electrodes are non-suitable for seawater desalination.[16, 37, 43, 67]

3.2. Origin of permselective ion electrosorption in subnanometer pores

To better understand the mechanism of permselective ion electrosorption in subnanometer pores, we then explored the equilibrium in-pore distributions for ions and water molecules by simulations. The intricacies of the electrical double-layer structure at the electrolyte-electrode interface majorly govern the surface charge and the resulting salt adsorption capacity.[68, 69] **Figure 3** depicts the distributions of ions and water molecules inside non-charged and polarized pores of different size. When the electrode is at the potential of zero charge (PZC), shown in **Figure 3b**, K^+ or Cl^- ions are unable to enter pores of less than 0.6 nm, although the pore could be wetted, indicating such pores are fully ionophobic.[51, 70] For larger pores, ions are found already inside the pore, seeming larger pores with more ions. These could be further seen in *Supporting Information*, **Figure S8** that, as the pore size shrinks, the in-pore ion density decreases, suggesting that the pore electrode becomes more ionophobic and ultimately fully ionophobic. When pores get either negatively or positively polarized (**Figure 3a,c**), for fully ionophobic pores (<0.6 nm) counter-ions move into the pore and accumulate in its central region; when pores get more ionophilic (>0.6 nm), the electrical double-layer inside the pores

becomes rich in counter-ions, and some co-ions are expelled. Moreover, multiple layers of ions, rather than one layer dwelling at the central part of the pores, are formed inside these large pores. Although their size is larger than K^+ cations in bare but similar in full hydration,[50] Cl^- anions reside closer to the slit wall than cations, suggesting a more fractured hydration shell than that of K^+ ions.

The distribution of in-pore water molecules is strongly influenced by the in-pore ions due to the hydration effect under nanopore confinement. Specifically, in fully ionophobic pores the pure water packing at PZC should be changed by ions electro-adsorbed under polarization; in more ionophilic pores, the adsorbed layer of water distributions in the positive side is higher but thinner than that in the negative side (**Figure 3a,c**). To further investigate the microstructures of the water molecules surrounding an ion inside the micropores, we show in **Figure 4** the radial distribution functions (RDFs) and the cumulative distribution functions (CDFs) between in-pore ions and their surrounding water molecules as well as the corresponding number density and angular distributions of water around an ion at its peak positions (i.e., the closest peak to the pore wall, **Figure 3**). Focusing on the K^+ ion at the negatively charge micropores (**Figure 4a**), we see that the coordination number of water molecules decreases as the pore becomes narrow; the value is around 4.8 and 7.6, respectively, for fully ionophobic pores (0.47 nm and 0.57 nm) and the other pores. From the pseudo-two-dimensional water number density near a K^+ (the upper row of **Figure 4c**), we observe that in subnanometer pores water is mainly located along the length of the pore on the top (or below, which is not shown due to the symmetry of data) of the ion, but not between the ion and the pore wall, as observed in **Figure 3** with only one layer of water and ions in such small pores. For a 0.77 nm pore, water in the hydration shell of a K^+ ion starts to more surround the cation, and for 0.97 nm pore, we see the emergence of more completed hydration shell. Finally, larger micropores (1.37 and 1.77 nm in *Supporting Information*, **Figure S9**) show an almost full hydration shell of K^+ ions.

The number of water molecules coordinating a K^+ ion in bulk simulation of 2 M KCl solution is found to be 6.7 (*Supporting Information*, **Figure S9**). The comparison between such coordination numbers for ions in bulk and in pore suggests that K^+ ions in fully ionophobic pores (0.47 nm and 0.57 nm) get partially dehydrated while K^+ ions in the less ionophobic pores become more hydrated with their hydration shells deformed concomitantly, which makes the water shell become denser and results in a higher coordination number. Such

deformations of hydration-shell structures can also be revealed by the pseudo-2D water angular distribution analysis near a K^+ ion (the lower row of **Figure 4c**), in which we compute the averaged angle formed by a water dipole and ion-oxygen vector for the ion with its hydrated water. For pores smaller than 0.97 nm, the orientation of water in the first layer of the hydration shell surrounding K^+ is majorly less than 45°, indicating that most water molecules are strongly aligned with preference of their dipoles pointing oppositely to its hydrated K^+ ion; when pore size is no less than 0.97 nm, water located between the K^+ ion and the pore wall is distorted, with a larger averaged angle (about 60°). Considering the co-ion (Cl^-) at negative polarization (*Supporting Information*, **Figure S10**) in pores of 0.97 nm or larger, the structures of the surrounding water molecules are nearly identical to those in bulk region, as well as both have a similar coordination number of 6.6. This aligns with the screening of the charged electrode by counter-ions and water so that most co-ions lay far from the pore surfaces.

We further investigated the state of water around a Cl^- ion confined in a positively polarized micropore. It can be observed that regardless of the pore size, Cl^- ions prefer to be adsorbed to the electrified pore wall comparing with K^+ ions (**Figure 3c** and the upper row of **Figure 4d**) while their hydration shell becomes more deformed with the pore size decreasing (lower row of **Figure 4d**). In terms of RDFs and CDFs, it could be found that the coordination numbers of water are about 5.5 for two small and fully ionophobic nanopores (0.47 nm and 0.57 nm) and approximately 7.0 for the other larger pores. Thereby, except fully ionophobic pores, water molecules in hydration shell get rearranged without ion dehydration, since the coordination number remains close to the bulk value. This phenomenon can be found even in the absence of an applied potential, suggesting that the hydration of the Cl^- ion changes little by the nanoconfinement. Moreover, the angular distributions of water in the first hydration shell has an averaged value of around 125°, indicating that one H-O bond of the water rather than the revert of water dipole points to the Cl^- ion (lower row of **Figure 4d**). These results imply a looser hydration shell of a Cl^- compared with that of a K^+ ion.

As the pore size increases, the pore becomes more ionophilic so that ions are more willing to get into the pore even in the absence of applied electrode potential (*Supporting Information*, **Figure S8**). In our experiments, the value of ~1 nm seems to be the boundary of pore size of micropores that whether they can be used for desalination or not. Correspondingly in simulations, pores with pore size obviously smaller than 1 nm are less ionophilic (*Supporting*

Information, **Figure S8**), because the entering-ions would experience confinement-caused dehydration in the aqueous solution. On the other hand, the degree of confinement has a significant impact on the dynamics of ions. Indeed, the diffusion coefficients of cation and anion inside a charged pore are much lower than their bulk values ($1.72 \cdot 10^{-9}$ m^2/s and $1.32 \cdot 10^{-9}$ m^2/s for Na^+ and Cl^-, respectively). Also, as pore size shrinks, the in-pore ions diffuse more slowly (*Supporting Information*, **Figure S11**), which can be attributed to their more deformed hydration shells under stronger confinement (**Figure 4**). However, the structure of water in hydration shells shows a negligible difference when the pore size exceeds 1.0 nm (**Figure 4** and *Supporting Information*, **Figure S9-10**).

3.3. Nuclear magnetic resonance spectroscopy

To correlate the molecular dynamics predictions on the ionophobicity, we carried out ^{1}H and ^{23}Na solid-state NMR after having soaked the samples in aqueous 800 mM NaCl; we selected ^{23}Na due to the experimental difficulties of observing the low-sensitivity ^{39}K nucleus, which is the only NMR-observable isotope of potassium. For better comparability, considering the influence of the particle size, we investigated the spectra of the ACC samples. As seen from the ^{1}H-NMR spectra in **Figure 5a**, all ACC samples show much narrower ^{1}H in-pore peaks relative to typical samples activated after crushing pyrolytic carbon sludges. This is due to the fibers having a narrow thickness distribution of modal width less than 100 micrometers, allowing for very homogeneous activation. The peaks become slightly broader with activation time due to small but inevitable activation inhomogeneities. The ^{23}Na spectra show that the amount of sodium very strongly decreases as the pore size is decreased (**Figure 5b**). The overall larger peak width of ^{23}Na compared to ^{1}H results from faster transverse relaation which could suggest slower sodium diffusion. Using the integral peak intensities in Topspin Software, we see that the measured in-pore sodium for ACC-0.59, ACC-0.67, ACC-0.88 and ACC-1.26 corresponds to 1%, 7%, 15%, and 23%, respectively, of the total measured ^{23}Na signal for each sample. Therefore, the proportion of the sodium ions that spontaneously enter the pores is very small for the smallest pore sizes (*i.e.*, they are ionophobic), whereas this increases as the pore size is increased. The strong decrease in sodium in sub-1-nm pores is in alignment with a recent study by Cervini *et al*.[35] and agrees with our molecular dynamics results.

4. Conclusions

We have investigated the performance of water desalination by micropores (including subnanometer pores) in aqueous media with high molar strength by both modeling and experiment. In contrast to the state-of-the-art CDI techniques, our results demonstrate the ability of subnanometer pores for permselective counter-ion electro-adsorption. This ability enables the use of such carbon electrodes with the need for an ion exchange membrane for CDI of saline media with seawater concentration levels of dissolved ions, as documented for KCl and NaCl in this work. This ability is lost once the pore size approaches and exceeds the 1-nm-range. Molecular dynamics simulations revealed that as the pore size of the electrode decreases, the pore becomes more ionophobic and the ion electrosorption mechanism shifts from non-permselective ion swapping to permselective counter-ion electro-adsorption, increasing the charge efficiency and desalination capacity of the system. In particular, the fully ionophobic pores exhibit complete permselectivity of counter-ions. These phenomena reflect the in-pore electrical double layer, especially the structures of water in the hydration shell of an ion. The increased ionophobicity with small size also aligns with the work that studied polyether-ether-ketone-derived small micropores via NMR spectroscopy (Ref. [35]) and our own NMR results. The findings reported here render a new path for CDI of saline water and briny water and call attention to turn again to porous carbons for CDI, based upon the permselective ion electrosorption of subnanometer pores.

Acknowledgments

G.F., S.B., and M.T.M. acknowledge the funding support from the National Natural Science Foundation of China (51876072, 51836003) and the Fundamental Research Funds for the Central Universities (2019kfyXMBZ040). V.P. and Y.Z. thank Eduard Arzt (INM) for his continuing support. S.B. also acknowledges the financial support from the China Scholarship Council. The computation was accomplished using the Tianhe II supercomputer in the National Supercomputing Center in Guangzhou, China. J.G. and L.C. acknowledge EPSRC and Johnson Matthey plc for the provision of an iCASE studentship. We also thank Lancaster University and the European Regional Development Fund (ERDF) for the provision of characterisation facilities under the Collaborative Technology Access Program (cTAP).

Author contributions

G.F. and V.P. conceptualized the work. S.B. and M.T.M. carried out the simulation and Y.Z. for the experiment. S.B., V.P., and G.F. analyzed the data. L.C. carried out NMR experiments and and L.C. and

J.G. analyzed NMR data. All authors engaged in discussions and writing of the manuscript.

Supporting Information

Data for the molecular dynamics simulation setup, characterization of carbons and cell setup, desalination performance measurements with aqueous NaCl solution, Basic electrochemical characterization, In-pore ions under different polarizations, water distribution surrounding ions in bulk and inside large pores

Conflict of interest

The authors declare no conflict of interest.

Figures

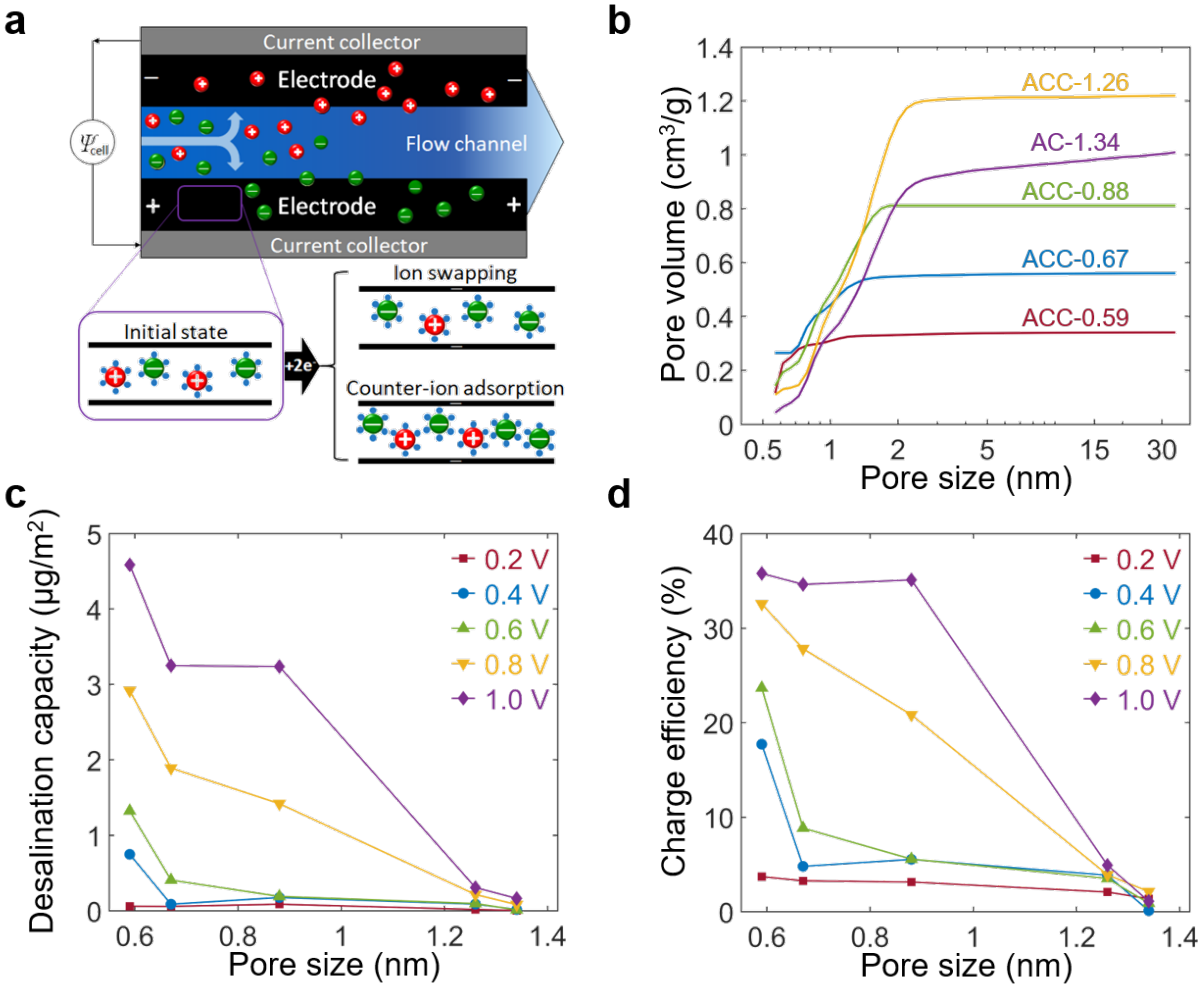

Figure 1. Capacitive deionization (CDI) of microporous carbons. a, The schematic figure for a CDI cell using porous carbon electrodes. Charge storage, generally, can be accomplished by permselective counter-ion electrosorption or non-permselective concurrence of co-ion desorption and counter-ion electro-adsorption (ion swapping). **b,** Cumulative pore size distribution obtained from nitrogen gas sorption isotherms at -196 °C, calculated by applying quenched solid density functional theory (QSDFT) and assuming pores have slit shape. **c-d**, Desalination capacity (**c**) and charge efficiency (**d**) obtained from CDI experiments on carbon electrodes with different average pore sizes. Experiments were carried out in aqueous 800 mM KCl.

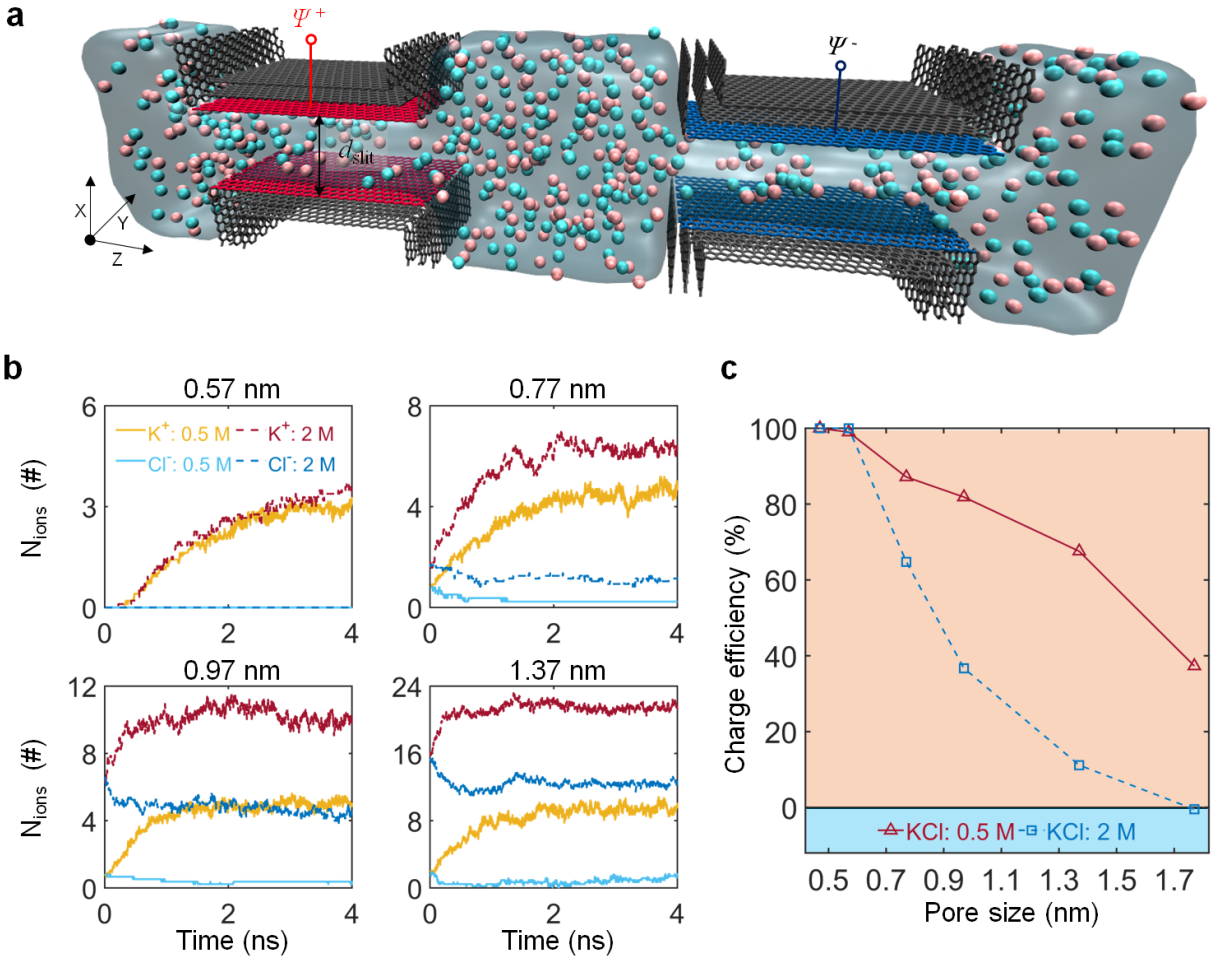

Figure 2. Molecular understanding of ion permselectivity by micropores. a, Schematics of the molecular dynamics simulation setup. The pore size, d_{slit}, is defined by the accessible gap between the surfaces of two inner graphene sheets, ranging from 0.47 nm to 1.77 nm, and the slit length is 5.84 nm along the Z-direction. The dimensions of the simulation system are d_{slit}+3.53 nm, 3.00 nm, and 5.84 nm. A constant potential drop is applied at the red, and blue labeled carbon atoms, in which red represents positive electrode, and blue represents the negative electrode. The applied voltage between the positive and negative electrode is set at 1.0 V. **b**, Time evolution of the number of cation and anion in the negatively charged micropores. Dark red and blue solid lines are, respectively, results for the cation and anion at 2 M molar concentration. Yellow and light blue dashed lines are for cation and anion at 0.5 M molar concentration. These results are evaluated during the charging simulations of each micropore. **c**, Charge efficiency, as a function of pore size. Red solid and dashed lines with triangle markers represent results of micropores in aqueous 0.5 M and 2 M KCl solutions, respectively.

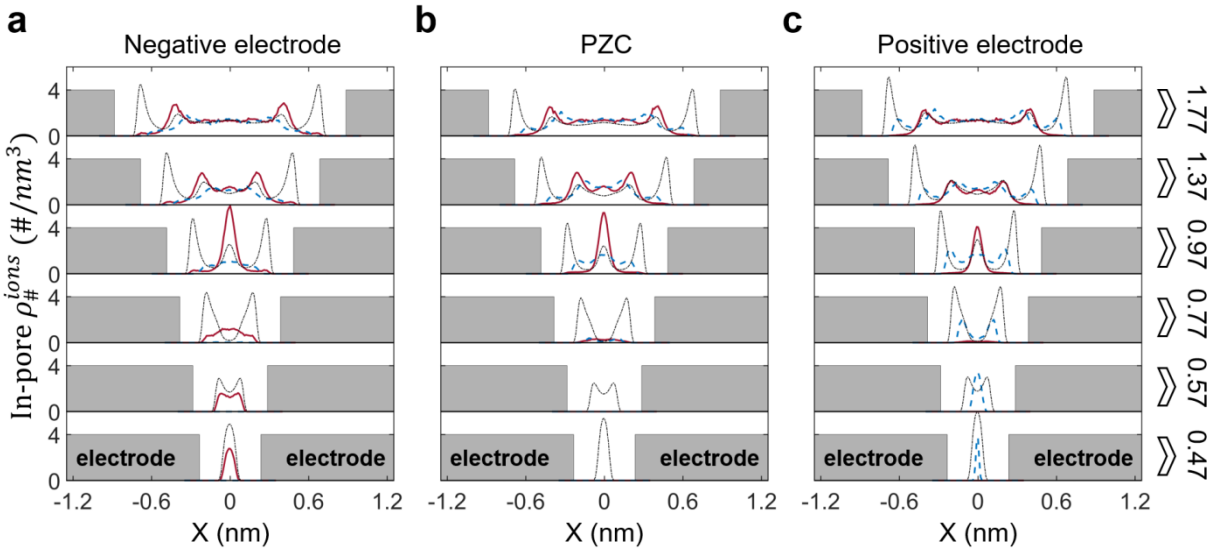

Figure 3. Ion and water distributions in micropores. **a-c,** Data in (**a**) and (**c**), respectively, show the number densities of ions and water in the negatively charged micropores and positively charged micropores, for a potential difference of 1.0 V between the two electrodes. Data shown in (**b**) represent the uncharged pore (i.e., at PZC). Red solid, blue dashed, and black dash-dotted cures are results for cations, anions, and water molecules, respectively. The number density of water shown here is scaled by 1/30 for better illustration. X = 0 corresponds to the central position of the pore.

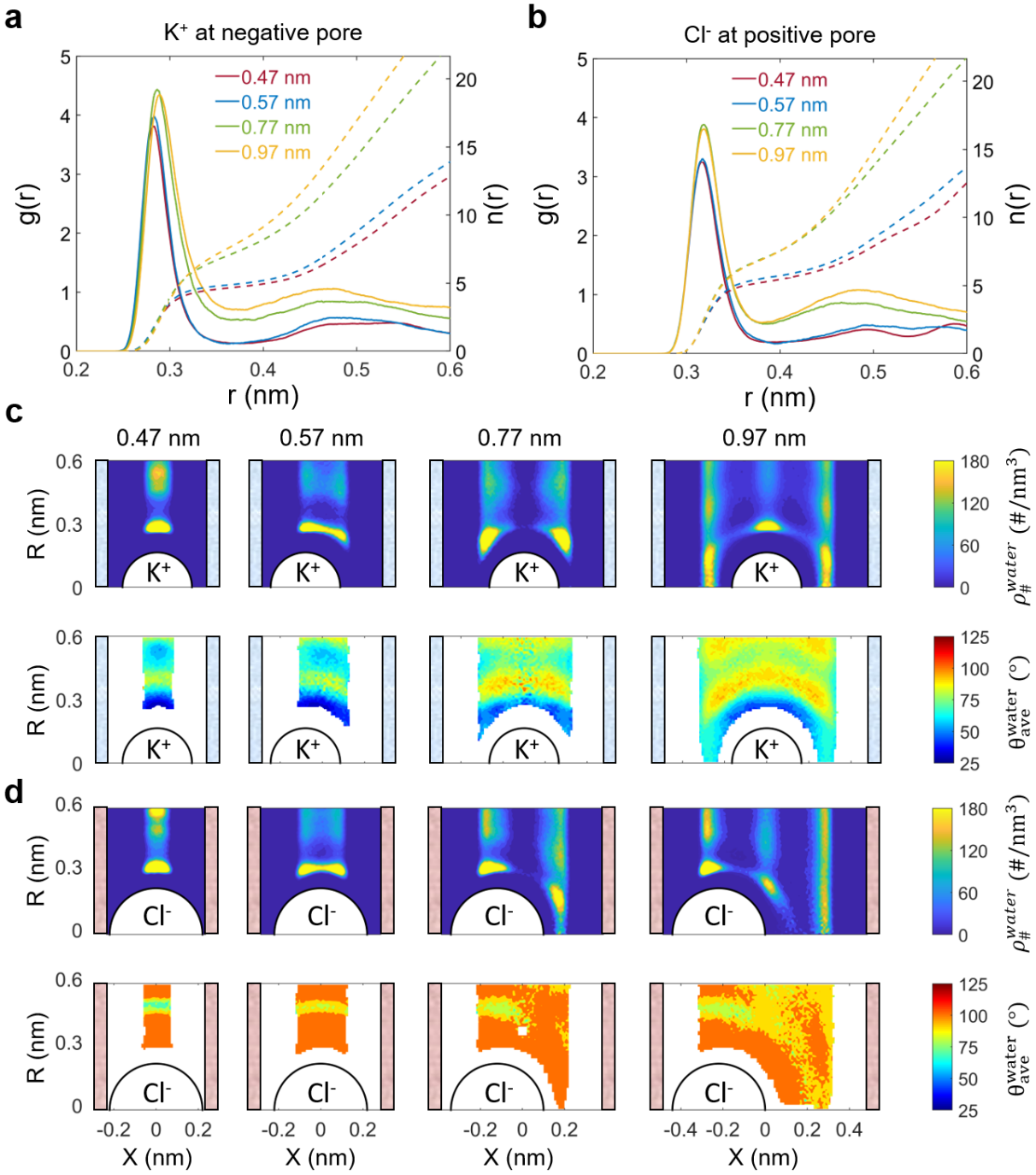

Figure 4. Structure of hydration shells of ions in polarized micropores. a-b, Radial distribution function, g(r) (solid lines, left Y-axis), and cumulative distribution function, n(r) (dashed lines, right Y-axis) of hydrated K^+ ions (**a**) and Cl^- ions (**b**) in negatively and positively polarized pores, respectively. The applied electrical potential difference between two electrodes is set as 1.0 V. The cumulative distribution function, n(r), is calculated by $n(r) = 4\pi\rho \int g(r)r^2 dr$, where ρ is the water density in the reservoir. **c-d,** Pseudo-2D number density (upper panel) and orientation (lower panel) distributions of water molecules around a K^+ ion (**c**) and a Cl^- ion (**d**) in micropores of different pore sizes under negative and positive polarization, respectively.

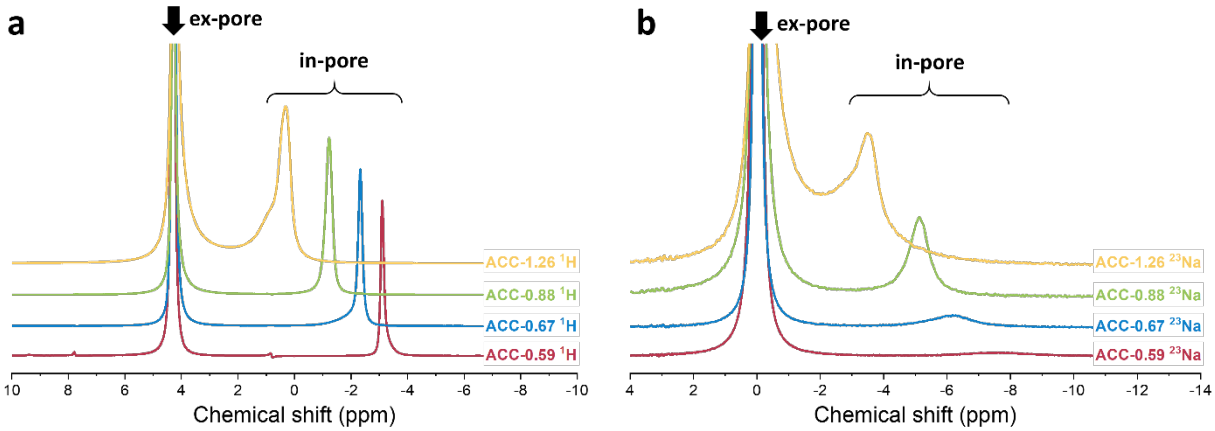

Figure 5. Solid-state nuclear magnetic resonance spectra after soaking the samples in aqueous 800 mM NaCl. a, ^{1}H spectra. **b**, ^{23}Na spectra.

References

1. M. Elimelech and W. A. Phillip, *Science*, 2011, **333**, 712-717.
2. M. A. Shannon, P. W. Bohn, M. Elimelech, J. G. Georgiadis, B. J. Marinas and A. M. Mayes, *Nature*, 2008, **452**, 301-310.
3. G. W. Murphy and J. H. Tucker, *Desalination*, 1966, **1**, 247-259.
4. Y. Oren, *Desalination*, 2008, **228**, 10-29.
5. R. Zhao, S. Porada, P. M. Biesheuvel and A. van der Wal, *Desalination*, 2013, **330**, 35-41.
6. A. Subramani and J. G. Jacangelo, *Water Res*, 2015, **75**, 164-187.
7. M. E. Suss, S. Porada, X. Sun, P. M. Biesheuvel, J. Yoon and V. Presser, *Energ Environ Sci*, 2015, **8**, 2296-2319.
8. G. Amy, N. Ghaffour, Z. Li, L. Francis, R. V. Linares, T. Missimer and S. Lattemann, *Desalination*, 2017, **401**, 16-21.
9. J. R. Miller, *Science*, 2012, **335**, 1312-1313.
10. M. Salanne, B. Rotenberg, K. Naoi, K. Kaneko, P. L. Taberna, C. P. Grey, B. Dunn and P. Simon, *Nature Energy*, 2016, **1**, 16070.
11. Y. Shao, M. F. El-Kady, J. Sun, Y. Li, Q. Zhang, M. Zhu, H. Wang, B. Dunn and R. B. Kaner, *Chemical Reviews*, 2018, **118**, 9233-9280.
12. M. A. Anderson, A. L. Cudero and J. Palma, *Electrochimica Acta*, 2010, **55**, 3845-3856.
13. S. I. Jeon, J. G. Yeo, S. Yang, J. Choi and D. K. Kim, *Journal of Materials Chemistry A*, 2014, **2**, 6378-6383.
14. F. Chen, Y. Huang, L. Guo, L. Sun, Y. Wang and H. Y. Yang, *Energ Environ Sci*, 2017, **10**, 2081-2089.
15. Z.-H. Huang, Z. Yang, F. Kang and M. Inagaki, *Journal of Materials Chemistry A*, 2017, **5**, 470-496.
16. S. Porada, R. Zhao, A. van der Wal, V. Presser and P. M. Biesheuvel, *Progress in Materials Science*, 2013, **58**, 1388-1442.
17. F. Perreault, A. Fonseca de Faria and M. Elimelech, *Chem Soc Rev*, 2015, **44**, 5861-5896.
18. L. Zou, G. Morris and D. Qi, *Desalination*, 2008, **225**, 329-340.
19. S. Porada, F. Schipper, M. Aslan, M. Antonietti, V. Presser and T.-P. Fellinger, *Chemsuschem*, 2015, **8**, 1867-1874.
20. P. Y. Liu, T. T. Yan, L. Y. Shi, H. S. Park, X. C. Chen, Z. G. Zhao and D. S. Zhang, *Journal of Materials Chemistry A*, 2017, **5**, 13907-13943.
21. X. Xu, L. Pan, Y. Liu, T. Lu, Z. Sun and D. H. C. Chua, *Scientific Reports*, 2015, **5**, 8458.
22. H. B. Li, L. D. Zou, L. K. Pan and Z. Sun, *Environ Sci Technol*, 2010, **44**, 8692-8697.
23. K. Dai, L. Shi, J. Fang, D. Zhang and B. Yu, *Materials Letters*, 2005, **59**, 1989-1992.
24. Y. Wimalasiri and L. Zou, *Carbon*, 2013, **59**, 464-471.
25. J. Biener, M. Stadermann, M. Suss, M. A. Worsley, M. M. Biener, K. A. Rose and T. F. Baumann, *Energ Environ Sci*, 2011, **4**, 656-667.
26. J. Chmiola, G. Yushin, Y. Gogotsi, C. Portet, P. Simon and P. L. Taberna, *Science*, 2006, **313**, 1760-1763.
27. S. Porada, L. Borchardt, M. Oschatz, M. Bryjak, J. S. Atchison, K. J. Keesman, S. Kaskel, P. M. Biesheuvel and V. Presser, *Energ Environ Sci*, 2013, **6**, 3700-3712.

28. C. Prehal, D. Weingarth, E. Perre, R. T. Lechner, H. Amenitsch, O. Paris and V. Presser, *Energ Environ Sci*, 2015, **8**, 1725-1735.

29. S. Kondrat, C. R. Perez, V. Presser, Y. Gogotsi and A. A. Kornyshev, *Energ Environ Sci*, 2012, **5**, 6474-6479.

30. C. Prehal, C. Koczwara, H. Amenitsch, V. Presser and O. Paris, *Nature Communications*, 2018, **9**, 4145.

31. M. Deschamps, E. Gilbert, P. Azais, E. Raymundo-Piñero, M. R. Ammar, P. Simon, D. Massiot and F. Béguin, *Nature Materials*, 2013, **12**, 351-358.

32. A. C. Forse, J. M. Griffin, C. Merlet, P. M. Bayley, H. Wang, P. Simon and C. P. Grey, *Journal of the American Chemical Society*, 2015, **137**, 7231-7242.

33. C. Merlet, C. Pean, B. Rotenberg, P. A. Madden, B. Daffos, P. L. Taberna, P. Simon and M. Salanne, *Nature Communications*, 2013, **4**, 2701.

34. C. Prehal, C. Koczwara, N. Jäckel, A. Schreiber, M. Burian, H. Amenitsch, M. A. Hartmann, V. Presser and O. Paris, *Nature Energy*, 2017, **2**, 16215.

35. L. Cervini, O. D. Lynes, G. R. Akien, A. Kerridge, N. S. Barrow and J. M. Griffin, *Energy Storage Materials*, 2019, **21**, 335-346.

36. J. M. Griffin, A. C. Forse, H. Wang, N. M. Trease, P. L. Taberna, P. Simon and C. P. Grey, *Faraday Discussions*, 2015, **176**, 49-68.

37. P. M. Biesheuvel, S. Porada, M. Levi and M. Z. Bazant, *J Solid State Electr*, 2014, **18**, 1365-1376.

38. M. A. Ahmed and S. Tewari, *Journal of Electroanalytical Chemistry*, 2018, **813**, 178-192.

39. Y. Cheng, Z. Hao, C. Hao, Y. Deng, X. Li, K. Li and Y. Zhao, *RSC Advances*, 2019, **9**, 24401-24419.

40. T. Kim and J. Yoon, *RSC Advances*, 2015, **5**, 1456-1461.

41. Y. Liu, C. Y. Nie, X. J. Liu, X. T. Xu, Z. Sun and L. K. Pan, *RSC Advances*, 2015, **5**, 15205-15225.

42. P. Srimuk, J. Lee, S. Fleischmann, S. Choudhury, N. Jäckel, M. Zeiger, C. Kim, M. Aslan and V. Presser, *Journal of Materials Chemistry A*, 2017, **5**, 15640-15649.

43. X. Gao, S. Porada, A. Omosebi, K.-L. Liu, P. M. Biesheuvel and J. Landon, *Water Res*, 2016, **92**, 275-282.

44. M. E. Suss and V. Presser, *Joule*, 2018, **2**, 10-15.

45. K. Singh, S. Porada, H. D. de Gier, P. M. Biesheuvel and L. C. P. M. de Smet, *Desalination*, 2019, **455**, 115-134.

46. M. Pasta, C. D. Wessells, Y. Cui and F. La Mantia, *Nano Letters*, 2012, **12**, 839-843.

47. J. Lee, S. Kim, C. Kim and J. Yoon, *Energ Environ Sci*, 2014, **7**, 3683-3689.

48. R. K. Kalluri, D. Konatham and A. Striolo, *The Journal of Physical Chemistry C*, 2011, **115**, 13786-13795.

49. R. K. Kalluri, M. M. Biener, M. E. Suss, M. D. Merrill, M. Stadermann, J. G. Santiago, T. F. Baumann, J. Biener and A. Striolo, *Physical Chemistry Chemical Physics*, 2013, **15**, 2309-2320.

50. E. R. Nightingale, *The Journal of Physical Chemistry*, 1959, **63**, 1381-1387.

51. S. Kondrat and A. Kornyshev, *The Journal of Physical Chemistry C*, 2013, **117**, 12399-12406.

52. G. Feng and P. T. Cummings, *The Journal of Physical Chemistry Letters*, 2011, **2**, 2859-2864.

53. L. Martínez, R. Andrade, E. G. Birgin and J. M. Martínez, *J Comput Chem*, 2009, **30**, 2157-2164.

54. W. D. Cornell, P. Cieplak, C. I. Bayly, I. R. Gould, K. M. Merz, D. M. Ferguson, D. C. Spellmeyer, T.

Fox, J. W. Caldwell and P. A. Kollman, *Journal of the American Chemical Society*, 1995, **117**, 5179-5197.

55. D. E. Smith and L. X. Dang, *The Journal of Chemical Physics*, 1994, **100**, 3757-3766.
56. H. J. C. Berendsen, J. R. Grigera and T. P. Straatsma, *The Journal of Physical Chemistry*, 1987, **91**, 6269-6271.
57. S. K. Reed, P. A. Madden and A. Papadopoulos, *The Journal of Chemical Physics*, 2008, **128**, 124701.
58. C. Merlet, B. Rotenberg, P. A. Madden, P. L. Taberna, P. Simon, Y. Gogotsi and M. Salanne, *Nature Materials*, 2012, **11**, 306-310.
59. J. Vatamanu, O. Borodin and G. D. Smith, *Journal of the American Chemical Society*, 2010, **132**, 14825-14833.
60. S. Bi, R. Wang, S. Liu, J. Yan, B. Mao, A. A. Kornyshev and G. Feng, *Nature Communications*, 2018, **9**, 5222.
61. C. Péan, C. Merlet, B. Rotenberg, P. A. Madden, P.-L. Taberna, B. Daffos, M. Salanne and P. Simon, *Acs Nano*, 2014, **8**, 1576-1583.
62. B. Hess, C. Kutzner, D. van der Spoel and E. Lindahl, *J Chem Theory Comput*, 2008, **4**, 435-447.
63. C. Kim, P. Srimuk, J. Lee, S. Fleischmann, M. Aslan and V. Presser, *Carbon*, 2017, **122**, 329-335.
64. M. Thommes, K. Kaneko, A. V. Neimark, J. P. Olivier, F. Rodriguez-Reinoso, J. Rouquerol and K. S. W. Sing, *Pure Appl Chem*, 2015, **87**, 1051-1069.
65. A. V. Neimark, Y. Lin, P. I. Ravikovitch and M. Thommes, *Carbon*, 2009, **47**, 1617-1628.
66. K. Gopinadhan, S. Hu, A. Esfandiar, M. Lozada-Hidalgo, F. C. Wang, Q. Yang, A. V. Tyurnina, A. Keerthi, B. Radha and A. K. Geim, *Science*, 2019, **363**, 145.
67. K. Tang, Y.-h. Kim, J. Chang, R. T. Mayes, J. Gabitto, S. Yiacoumi and C. Tsouris, *Chem Eng J*, 2019, **357**, 103-111.
68. J. Chmiola, C. Largeot, P.-L. Taberna, P. Simon and Y. Gogotsi, *Angewandte Chemie International Edition*, 2008, **47**, 3392-3395.
69. G. Feng, R. Qiao, J. Huang, B. G. Sumpter and V. Meunier, *Acs Nano*, 2010, **4**, 2382-2390.
70. S. Kondrat, P. Wu, R. Qiao and A. A. Kornyshev, *Nature Materials*, 2014, **13**, 387-393.